



An advanced NiFe-LDH nanoclusters arrays for high-efficient full water splitting

Jinjin Ding^{1,2}, Mengke Zhang^{1,2}, Xiaoqing Wei¹, Wenwu Song¹, Jin Wang^{1,2,*} ,
Tongming Sun^{1,2}, Jinli Zhu^{1,2,*}, and Minmin Wang^{1,2,*}

¹School of Chemistry and Chemical Engineering, Nantong University, Nantong 226019, China

²Nantong Key Laboratory of Intelligent and New Energy Materials, Nantong University, Nantong 226019, China

Received: 11 May 2021

Accepted: 14 August 2021

Published online:
25 August 2021

© The Author(s), under
exclusive licence to Springer
Science+Business Media, LLC,
part of Springer Nature 2021

ABSTRACT

A rational structural strategy to design rambutan-like NiFe-LDH nanocluster arrays electrode via a buffer-salt-assisted hydrothermal method was reported. For our developed electrode, large stable current density of 100 and 200 mA cm⁻² at overpotential of only 283 and 300 mV in oxygen evolution reaction in alkaline electrolyte was obtained, which is dramatically lower than many previous reported overpotentials. It also exhibits low Tafel slope at current range from 10 to 25 mA cm⁻² (56.47 mV dec⁻¹). Further analysis demonstrates the key role of higher carriers of the rambutan-like NiFe-LDH nanocluster arrays electrode in boosting the water-splitting performance of the resulting system. Benefiting from the fine geometry shape of the self-supported nanocluster nanoarrays electrode, the transfer process of the reactants and oxygen/hydrogen bubbles is accelerated. In addition, a 19-time enhancement of carrier concentration for our developed rambutan-like NiFe-LDH nanoclusters (2.9 × 10²⁹ m⁻³) is obtained. Notably, the resultant rambutan-like NiFe-LDH nanocluster arrays electrode exhibits enhanced stability (in high and low current density) for the full water splitting in 1 M KOH, remaining nearly 100% of the original current density after continued testing for 20 h. This finding may provide new insight on rational structural design LDH nanostructures with high performance for electrocatalysis.

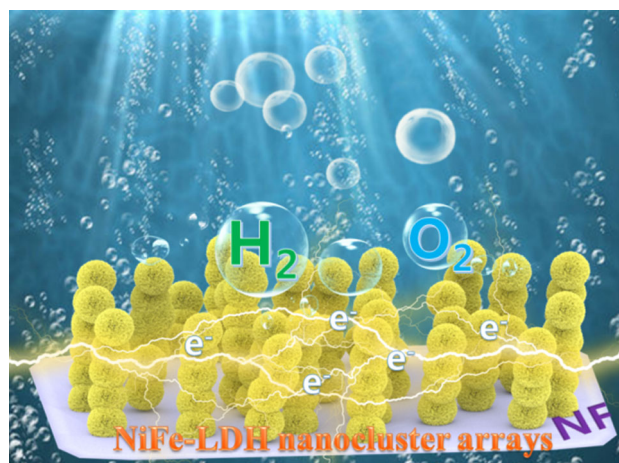
Handling Editor: Andrea de Camargo.

Jinjin Ding and Mengke Zhang contributed equally to this work.

Address correspondence to E-mail: wangjin110@ntu.edu.cn; jinlizhu@ntu.edu.cn; mmwang0528@ntu.edu.cn

GRAPHIC ABSTRACT

A highly hydrophilic NiFe-LDH nanocluster arrays electrode is developed for efficient full water splitting. Large and stable current density of 200 mA cm^{-2} is obtained at overpotential of 300 mV. Besides, the faraday efficiency is nearly 100%.



Introduction

Highly efficient electrocatalysts composed of earth-abundant elements are desired for water splitting to produce clean energy. Recently, attention has been distracted to non-noble metals such as first-row transition metal hydroxides/oxides compound, and it can catalyze the water splitting efficiently when compounded with other metals in the row [1–9]. In recent years, NiFe-layered double hydroxides (LDHs) consisting of positively charged layers and interlayer anions as 2D materials have showed the best OER catalytic activity in alkaline solution, which have attracted great attention [10–14]. The main challenges in designing LDH-based electrocatalysts for practical full water splitting primarily derive from the rigorous requirement of electron/holes transfer efficiency at large current densities. In recent years, many effective strategies have been reported to further enhance the water-splitting performance of NiFe-based electrocatalysts, such as optimizing the composition of Ni/Fe, introducing conductive components to enhance electron transfer ability [15–17], and

designing special morphologies to expose more active sites. Specifically, it is highly desired to realize the effect of two birds with one stone by rationally designing the geometry/shape of the layered structure, and this kind of electrode not only has high electron transfer efficiency but also can expose many active sites.

In general, ultrathin nanosheets structure is beneficial to expose massive catalytically active sites [18]. In addition, a fine nanoarray structure is demonstrated to facilitate bubble release and ion transfer because of its great reduction of the contact area between bubbles and the electrode [19–24]. Hence, we rationally design and synthesize a rambutan-like NiFe-LDH nanocluster arrays electrode via a buffer-salt-assisted hydrothermal method for enhancing water-splitting performance. The prominent structural feature of the as-obtained catalysts lies in the presence of ultrathin NiFe-LDH nanosheet nanostructures, endowing with the merits of not only facilitating the transmission of electrons but also exposing massive catalytically active edge sites. Meantime, the nanocluster array geometry structure can absorb liquid-phase electrolyte onto the electrode

surface due to its special capillary forces, which boosts the processes of mass transfer and electrolyte penetration [25, 26]. Also, the NiFe nanoalloy nanoparticles decorated at nanosheets increase the roughness of the catalysts, which is important for the access of reactants and the release of oxygen bubbles [27, 28]. Such material requires only overpotential (η) of 300 mV to achieve a geometrical current density of 200 mA cm⁻² in 1 M KOH solution and a ~19 times enhancement of carrier concentration for the as-prepared NiFe-LDH nanocluster arrays (2.9×10^{29} m⁻³) are obtained.

Experimental section

Materials

All chemicals were used directly without further purification. Cobalt (II) nitrate hexahydrate (AR, 99%), FeCl₃ (AR, 98%), urea (AR, 99%), NH₄F (AR, 98%), sodium citrate (98%), potassium hydroxide (AR, 90%) were purchased from Aladdin (Shanghai, China). Ultrapure water (18.5 MΩ cm⁻¹) was used throughout the whole experiment.

Synthesis of rambutan-like NiFe-LDH microspheres/NF samples

Typically, nickel foams (NF, 1 cm × 1 cm) were degreased by sonication immersed in ethanol, acetone, and isopropanol for 10 min, respectively. Then rinse with deionized water. Finally, the samples were dried in an oven at 60 °C for 12 h. The rambutan-like NiFe-LDH nanoclusters arrays were obtained by a one-step buffer-salt-assisted hydrothermal method. Specifically, 4 mmol Ni (NO₃)₂, 1 mmol FeCl₃, 7.5 mmol NH₄F, 16 mmol uric, and 0.75 mmol sodium citrate (abbreviated as SCT) were dissolved in 40 ml ultrapure water completely by ultrasound for 15 min, then transferred 30 mL of the above solution to 50 mL Teflon-lined stainless-steel autoclave. Sodium citrate acts as a buffer-salt. To perform chemical deposition of rambutan-like NiFe-LDH nanocluster array on NFs formation, the cleaned NF is placed vertically into a Teflon-lined stainless-steel autoclave and heated at 120 °C for 12 h. The precipitate was washed with water and ethanol three times and then dried in an oven at 60 °C for 24 h. For comparison, we synthesis the NiFe-LDH/NF

samples under the same conditions except for the addition of SCT.

Characterizations

The as-synthesized samples were examined by powder X-ray diffraction (PXRD, BRUKER AXS D8 Advance, radiation source Cu K α) at a 2θ range of 5–90° with scan speed 5°·min⁻¹. The morphology was observed on field emission scanning electron microscope (FESEM, ZEISS Gemini SEM 300) and transmission electron microscopy (TEM, JEOL JEM-2100). The construction and binding energies of the samples were studied by X-ray photoelectron spectroscopy (XPS).

Electrochemical measurements

All electrochemical tests were carried out on a traditional three-electrode system by electrochemical workstation (CHI 660E) at room temperature. Ag/AgCl (saturated KCl) was used as reference electrode, carbon rod as counter electrode, and as-prepared 1 cm × 1 cm NF-based electrodes as working electrode. Linear sweep voltammetry (LSV) curves toward OER were measured at a scan rate of 2 mV s⁻¹ after 100 cyclic voltammetry (CV) scans. For the CV experiments, we first stand the electrode in the electrolyte for 5–10 min to obtain the OCP) as activation in 1 M KOH (pH = 14.0). All the initial data were corrected for 80% iR loss and the potentials were transferred to a reversible hydrogen electrode (RHE) according to the formula of $E_{vs.RHE} = E_{vs.Ag/AgCl} + 0.197 \text{ V} + 0.059 \times \text{pH}$. Electrochemical impedance spectroscopy (EIS) was operated on the same three electrodes and 1 M KOH electrolyte, and the frequency range was from 0.01 to 10⁵ Hz, and the amplitude was 10 mV. The electrochemical surface area (ECSA) was calculated by CVs in different scan rates from 20 to 60 mV s⁻¹. Amperometry *i*-*t* curve was carried out in 1 M KOH to test the samples' stability. Mott-Schottky (M-S) curve used a three-electrode system with an applied frequency of 1 kHz and a potential amplitude of 10 mV/s. We obtain the Mott-Schottky (MS) relationship of the semiconductor space charge layer capacitance (C_{SC}) by the Mott-Schottky (MS) equation [29]:

$$\frac{1}{C_{SC}^2} = \frac{2}{eN_D\epsilon_0\epsilon} \left(E - E_{FB} - \frac{KT}{e} \right)$$

Carrier concentration (N_D , cm^{-3}) can be calculated using the slope of the Mott–Schottky curve [30]:

$$N_D = (2/e\epsilon_0\epsilon) [d(1/C_{SC}^2)/dE]^{-1}$$

E_{FB} is the flat band potential, $e = 1.6 \times 10^{-19}$ C, $\epsilon_0 = 8.85 \times 10^{-14}$ F/cm, ϵ is the permittivity of NiO (30).

The overall water-splitting performances were performed in a two-electrode system, and the prepared NiFe-LDH nanocluster arrays samples were worked as cathode and anode, respectively. The produced H_2 and O_2 were collected using a drainage method via a two-electrode water-splitting setting in 1200 s of test at 100 mA s^{-1} . In detail, the theoretical O_2 and H_2 yields were calculated by formula of $n(\text{O}_2) = Q/n \cdot F$ according to previous literature [31].

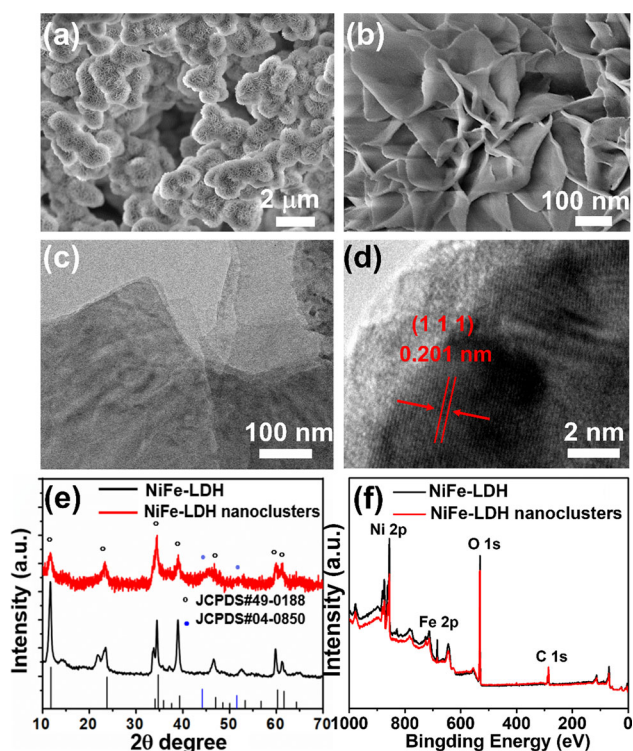


Figure 1 a, b SEM images of rambutan-like NiFe-LDH nanoclusters. c, d TEM and HRTEM images of rambutan-like NiFe-LDH nanoclusters. e, f The PXRD patterns and XPS spectra of NiFe-LDH and rambutan-like NiFe-LDH nanoclusters.

Results and discussion

The hydrophilic NiFe-LDH nanocluster arrays were prepared by a facile buffer-salt-assisted hydrothermal strategy, and the detailed synthesis methods are shown in the experiment section. The morphology of the as-prepared rambutan-like NiFe-LDH nanocluster arrays was characterized by SEM. In Fig. 1a and b, SEM images reveal that the resulting samples possess a 3D hierarchical structure, which self-assembled by numerous nanosheets to nanoclusters with diameters ~ 900 nm and the nanoclusters connected like a rosary to form nanocluster arrays. Such a nanoarray structure with strong capillary forces is beneficial to absorb electrolyte onto the electrode [32]. At the same time, the edges of the nanosheets are curled due to their ultrathin structure. The detailed microstructure of the as-prepared NiFe-LDH nanosheets was further determined by TEM (Fig. 1c). High-resolution TEM (HRTEM) was further performed to reveal the crystal structures of as-prepared NiFe-LDH nanocluster arrays. As shown in Fig. 1d, NiFe₃ alloy nanoparticles with a d-spacing of 0.201 nm (111) were distributed on the nanosheets. The detailed composition information was obtained by EDX and elemental mapping images (Fig. S1). Furthermore, PXRD measurements were conducted to determine the crystal structure of NiFe-LDH nanocluster arrays and traditional NiFe-LDH. As shown in Fig. 1e, both two samples showed typical diffraction peaks at reflections of NiFe-LDH phase with rhombohedral structure (JCPDS# 04-0188). Compared with the NiFe-LDH pattern, NiFe-LDH nanocluster arrays shown broader peak width and these patterns show typical sawtooth-shaped diffraction lines, with a sharp rise on the left side and asymmetry slop in the right. From the PXRD results, it is concluded that the SCT results in disordered stacking and the sufficient interlayer expansion of NiFe-LDH layers [33]. Two characteristic diffraction peaks located at 44.1° and 51.6° can be observed in the as-prepared rambutan-like NiFe-LDH nanoclusters which are indexed to NiFe nanoalloy (JCPDS#04-0850). PXRD patterns were further demonstrated that the SCT makes great influence on the crystal phase of NiFe-LDH microspheres (Fig. S2). The detailed information and discussion were shown in Supporting information section.

The elemental composition and electronic state of as-prepared samples were investigated by X-ray

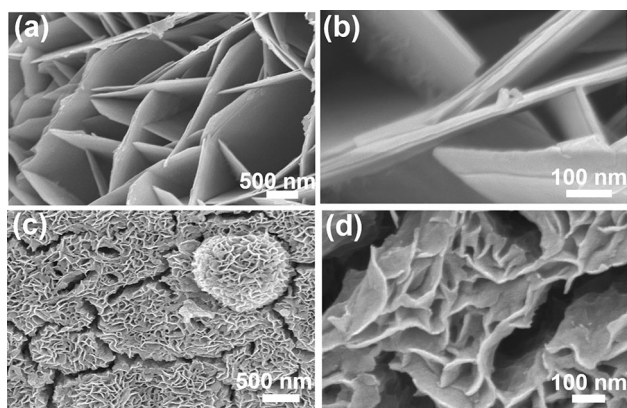


Figure 2 a, b SEM images of NiFe-LDH. c, d SEM images of NiFe-LDH which synthesized with assisting of 0.075 mM SCT.

photoelectron spectroscopy (XPS). As shown in Fig. 1f, the survey spectra revealed the presence of C, O, Fe, and Ni elements in both NiFe-LDH and NiFe-LDH nanocluster arrays, which demonstrated that the SCT makes no impact on the composition of the final product. The XPS results also demonstrated the existence of metallic state of Fe and Ni in the as-developed rambutan-like NiFe-LDH nanocluster (Fig. S3). The detailed information and discussion are shown in Supporting information section.

For comparison, we synthesized NiFe-LDH without SCT, as shown in Fig. 2a and b, the thickness of nanosheets was ~ 20 nm, and there are no nanoclusters generated. Meanwhile, SEM images for NiFe-LDH (0.075 mM SCT) show traditional sheet structure and the rambutan-like structure disappeared (Fig. 2c and d). To explore the potential growth mechanism of NiFe-LDH nanocluster arrays, pH values of the precursor solution of samples with and without SCT are shown in Fig. S4. For as-prepared NiFe-LDH nanocluster arrays, the pH value of precursor solution was 4.27, which was lower than the other samples. Therefore, the slow hydrolysis of SCT plays a great role in synthesizing rambutan-like NiFe-LDH nanocluster arrays. We use NiFe-LDH nanocluster arrays with 0.05 mM SCT for the following experiment. The as-prepared NiFe-LDH nanocluster arrays catalyst is also highly hydrophilic, as shown in Fig. S5, which is conducive to the transportation to the catalysts and gas diffusion for maintaining a continuous water supply for water splitting.

To examine the highly hydrophilic NiFe-LDH nanocluster arrays on the electrocatalytic water-

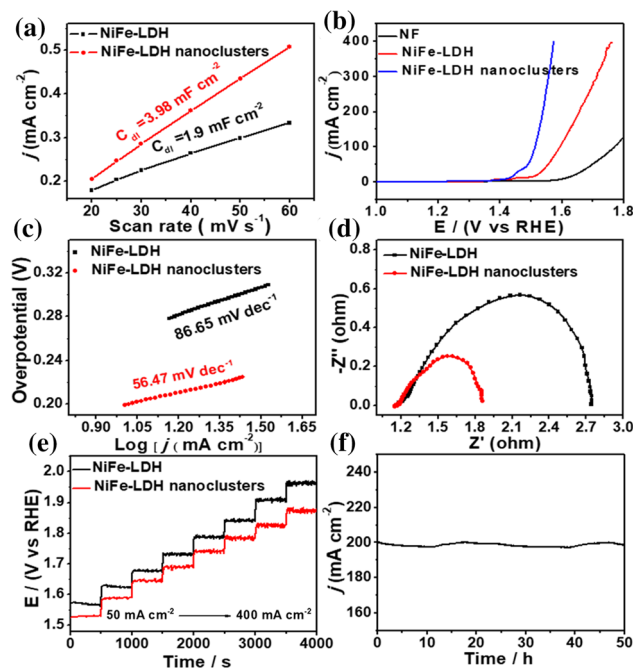


Figure 3 OER: a Plots of the capacitive current densities versus scan rate of NiFe-LDH and NiFe-LDH nanoclusters electrodes. b Linear sweep voltammetry curves of pure NF, NiFe-LDH and NiFe-LDH nanoclusters electrodes in 1 M KOH. c Tafel plots of NiFe-LDH and NiFe-LDH nanoclusters. d EIS plots for NiFe-LDH and NiFe-LDH nanoclusters electrodes at $\eta = 280$ mV in 1 M KOH. e Multi-step current process obtained for the NiFe-LDH and NiFe-LDH nanocluster arrays electrodes. f Time-dependent current density curves for the NiFe-LDH nanocluster arrays electrode at 200 mA cm^{-2} for 50 h.

splitting performance, electrochemical characterizations were carried out by a three-electrode system. Herein, the electrochemically active surface area (ECSA) was obtained from the formula $\text{ECSA} = C_{\text{dl}}/C_s$ according to previously reported literature [34], in which, a specific capacitance ($C_s = 0.040 \text{ mF cm}^{-2}$ in 1 M KOH solution) is used to calculate the ECSA based on the previous report by McCrory et al. [35] At the same time, C_{dl} denotes the electrochemical double-layer capacitance, which is measured using cyclic voltammetry (CV) curves at various scan rates (Fig. S6). As shown in Fig. 3a, the as-prepared NiFe-LDH nanocluster arrays exhibit high C_{dl} , and the ECSA values of NiFe-LDH and NiFe-LDH nanocluster arrays were calculated to be 47.5 cm^2 and 99.5 cm^2 , respectively. The higher ECSA of NiFe-LDH nanocluster arrays may attribute to the peculiar nanocluster array structure, facilitating exposing more active sites [36–39]. Polarization curves for the pure NF, NiFe-LDH, and NiFe-LDH nanocluster

arrays electrode at a scan rate of 2 mV s^{-1} are shown in Fig. 3b. The NiFe-LDH nanocluster arrays electrode showed higher current density and lower onset potential compared to NiFe-LDH electrode. Furthermore, the Tafel plots of NiFe-LDH and NiFe-LDH nanocluster arrays electrode with the linear regions are fitted with the Tafel equation. It also exhibits excellent reaction kinetics with low Tafel slope of $56.47 \text{ mV dec}^{-1}$ at current density range from 10 to 25 mA cm^{-2} , which is much lower than that of NiFe-LDH electrode ($86.65 \text{ mV dec}^{-1}$) (Fig. 3c). This electrochemical performance is higher than many previously reported NiFe-LDH electrocatalysts (Table S1). In order to further understand the rational structure strategy on the kinetics of OER, electrical impedance spectroscopy (EIS) was performed at the overpotential of 280 mV (Fig. 3d). Compared to the NiFe-LDH electrode, the NiFe-LDH nanoclusters array electrode exhibited lower charge transfer resistance in the low-frequency region in the Nyquist plot, which indicated favorable charge transport kinetics. At the same time, the stability and lower potential in the multi-step chronopotentiometry curve for the NiFe-LDH and NiFe-LDH nanocluster arrays electrode (Fig. 3e) and $i-t$ curves for the NiFe-LDH nanocluster arrays electrode at 200 mA cm^{-2} for 50 h (Fig. 3f) reflecting excellent mass transport and electrical conductivity, as well as the mechanical robustness of the electrode [40].

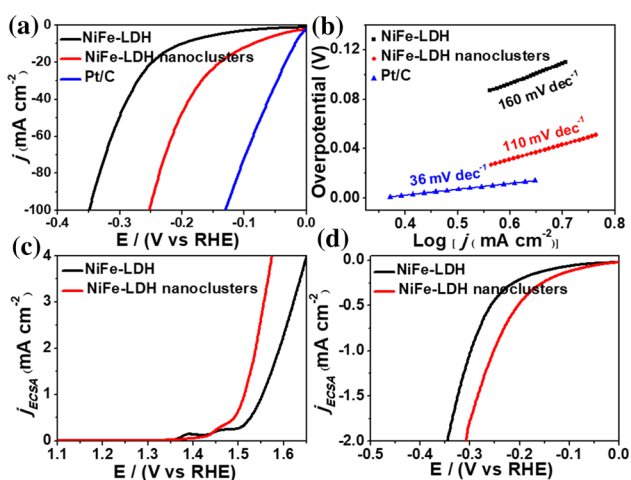


Figure 4 HER: **a** Polarization curves and corresponding **b** Tafel plot of the NiFe-LDH and NiFe-LDH nanocluster arrays electrodes at a scan rate of 2 mV s^{-1} . **c** OER and **d** HER performance based on ECSA for NiFe-LDH and NiFe-LDH nanocluster arrays, respectively.

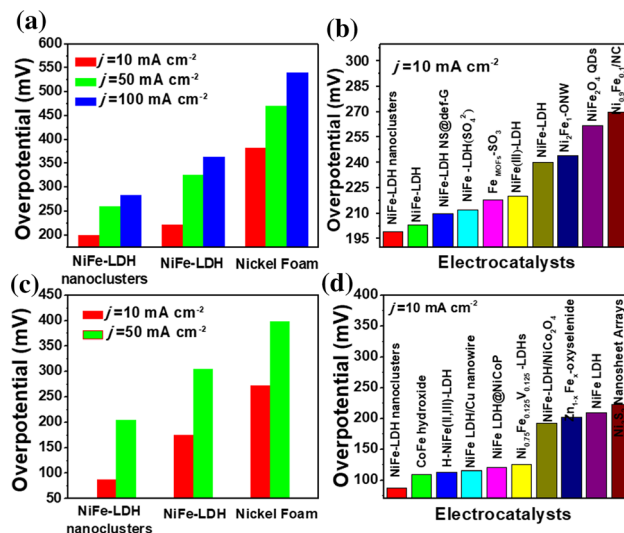


Figure 5 **a, c** OER and HER overpotentials of NiFe-LDH nanocluster arrays, NiFe-LDH, and nickel foam electrode at various current densities. **b, d** OER and HER overpotentials at current densities of 10 mA cm^{-2} for our prepared NiFe-LDH nanocluster arrays electrode and other previous reported electrodes [41–57].

We also tested the hydrogen generation performance of the as-prepared electrode. Figure 4a exhibits the polarization curves of NiFe-LDH and NiFe-LDH nanocluster arrays electrodes in 1 M KOH solution at a scan rate of 2 mV s^{-1} . Notably, the as-obtained NiFe-LDH nanocluster arrays electrode showed a significantly higher current density over the whole potential range and a lower $\eta = 137 \text{ mV}$ at the current density of 20 mA cm^{-2} than NiFe-LDH. Meanwhile, as shown in Fig. 4b, the NiFe-LDH nanocluster arrays electrode showed a lower Tafel slope of 110 mV dec^{-1} in the region of $\eta = 40\text{--}50 \text{ mV}$, which further manifests the enhanced kinetics in this hybrid nanosystem. The water-splitting performance based on ECSA also demonstrated the superiority of as-prepared NiFe-LDH nanocluster arrays electrodes in both OER and HER processes (Fig. 4c and d). As shown in Fig. 5, the as-prepared NiFe-LDH nanocluster arrays electrode exhibited a fairly excellent OER and HER performance compared with NiFe-LDH electrode and other previous reported electrodes.

The Mott–Schottky (M-S) analysis on as-prepared electrodes was also determined in Fig. S7, all samples exhibited a typical p-typed nature in their M-S curves with negative slopes. Importantly, the NiFe-LDH nanocluster arrays electrode showed substantially

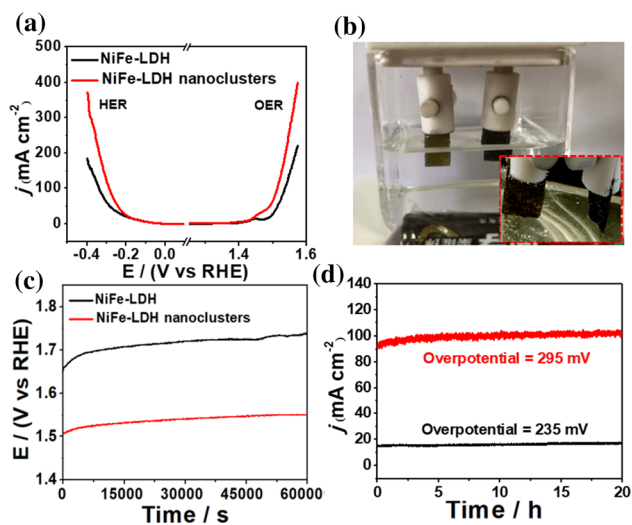


Figure 6 **a** Linear sweep voltammetry curves of overall water splitting for NiFe-LDH and NiFe-LDH nanocluster arrays electrodes at a scan rate of 5 mV s^{-1} . **b** Photos of the NF/NiFe-LDH nanoclusters array//NiFe-LDH nanoclusters array/NF electrolyze driven by a single 1.5 V AAA battery. **c** Chronopotentiometric curve of water electrolysis for NiFe-LDH and NiFe-LDH nanocluster arrays in a two-electrode configuration with a constant current density of 10 mA cm^{-2} . **d** Time-dependent current density curves for the NiFe-LDH nanocluster arrays electrode under static overpotential of 235 mV and 295 mV for 20 h.

smaller slopes in the M-S plot compared to the NiFe-LDH electrode. Meantime, based on the M-S analysis [30], the electrode carries of NiFe-LDH nanocluster arrays were calculated to be $2.9 \times 10^{29} \text{ m}^{-3}$, which is 19 times higher than the NiFe-LDH electrode ($1.58 \times 10^{28} \text{ m}^{-3}$). Meanwhile, the obtained NiFe-LDH nanocluster arrays electrode showed higher overall water-splitting performance than the NiFe-LDH electrode (Fig. 6a). Inspired by the good catalytic activities in both OER and HER, the NiFe-LDH nanocluster arrays catalyst was simultaneously employed as the anode and cathode to further assemble an electrolyze for overall water splitting in 1 M KOH aqueous solution. As shown in Fig. 6b and Video S1, the two same electrodes were connected to the cathode and anode of a single 1.5 V battery, respectively, and it was found that it can be used as a bifunctional catalyst to electrolyze water and generate numerous bubbles even at low potential. As shown in Fig. S8, only H_2 and O_2 gases with a molar ratio close to 2:1 are detected, and the Faradaic efficiency is determined to be 99.6% during water

electrolysis, demonstrating that water is completely decomposed into oxygen and hydrogen. Meanwhile, we also tested the long-term stability of the system for 60000 s in 1.0 M KOH solution. As shown in Fig. 6c, the potential showed slight changes, which indicating the NiFe-LDH nanocluster arrays electrode had superior stability in the long-term electrochemical process. To further explore the stability of catalytic materials at low and high current density, the catalytic materials were placed in 1 M KOH and tested by an *i*-*t* curve at a constant overpotential of 235 mV and 295 mV, the electrode retained current density $\sim 100\%$ after continued 20 h testing (Fig. 6d). The remarkable features of high activity, favorable kinetics, and strong durability suggest that the as-prepared rambutan-like NiFe-LDH nanocluster arrays electrode is a promising candidate to catalyze water splitting.

Conclusion

Summarily, a highly hydrophilic NiFe-LDH nanocluster arrays electrode was developed for highly efficient full water splitting. Benefiting from the fine geometry structure, the as-obtained NiFe-LDH nanocluster arrays electrode was improved in the properties of charge carriers transfer and kinetics of catalytic reactions. The as-obtained electrocatalyst exhibits excellent catalytic activity with the overpotential of 283 and 300 mV at 100 and 200 mA cm^{-2} , and a ~ 19 times enhancement of carrier concentration, as well as good durability. It also exhibits excellent reaction kinetics with a low Tafel slope of $56.47 \text{ mV dec}^{-1}$ at current density range from 10 to 25 mA cm^{-2} . Therefore, the simple buffer-salt-assisted structure designing strategies may open a new avenue to design heterogeneous nanostructures with high performance for electrocatalysis.

Acknowledgements

This work was supported by Natural Science Foundation of Jiangsu Province (BK20190918) and Natural Science Research Projects of Universities in Jiangsu Province (19KJB430030). We are also very grateful to the Nantong University Analytical Testing Center for its support for testing.

Declarations

Conflict of interest The authors declare that they have no conflict of interest.

Supplementary Information: The online version contains supplementary material available at <https://doi.org/10.1007/s10853-021-06451-7>.

References

- [1] Gorlin Y, Jaramillo TF (2010) A bifunctional nonprecious metal catalyst for oxygen reduction and water oxidation. *J Am Chem Soc* 132:13612. <https://doi.org/10.1021/ja104587v>
- [2] Dincă M, Surendranath Y, Nocera DG (2010) Nickel-borate oxygen-evolving catalyst that functions under benign conditions. *Proc Natl Acad Sci U.S.A.* 107:10337. <https://doi.org/10.1073/pnas.1001859107>
- [3] Esswein AJ, McMurdo MJ, Ross PN, Bell AT, Tilley TD (2009) Size-dependent activity of Co_3O_4 nanoparticle anodes for alkaline water electrolysis. *J Phys Chem C* 113:15068. <https://doi.org/10.1021/jp904022e>
- [4] Kanan MW, Nocera DG (2008) In situ formation of an oxygen-evolving catalyst in neutral water containing phosphate and Co^{2+} . *Science* 321:1072. <https://doi.org/10.1126/science.1162018>
- [5] Manikandan A, Ilango PR, Chen C-W, Wang Y-C, Shih Y-C, Lee L, Wang ZM, Ko H, Chueh Y-L (2018) A superior dye adsorbent towards the hydrogen evolution reaction combining active sites and phase-engineering of (1T/2H) $\text{MoS}_2/\alpha\text{-MoO}_3$ hybrid heterostructured nanoflowers. *J Mater Chem A* 6:15320. <https://doi.org/10.1039/C8TA02496K>
- [6] Wu C, Zhang J, Tong X, Yu P, Xu J-Y, Wu J, Wang ZM, Lou J, Chueh Y-L (2019) A critical review on enhancement of photocatalytic hydrogen production by molybdenum disulfide: from growth to interfacial activities. *Small* 15:1900578. <https://doi.org/10.1002/sml.201900578>
- [7] Ramalingam V, Varadhan P, Fu H-C, Kim H, Zhang D, Chen S, Song L, Ma D, Wang Y, Alshareef HN, He J-H (2019) Heteroatom-mediated interactions between ruthenium single atoms and an mxene support for efficient hydrogen evolution. *Adv Mater* 31:1903841. <https://doi.org/10.1002/adma.201903841>
- [8] Alarawi A, Ramalingam V, He J-H (2019) Recent advances in emerging single atom confined two-dimensional materials for water splitting applications. *Mater Today Energy* 11:1. <https://doi.org/10.1016/j.mtener.2018.10.014>
- [9] Sriram P, Manikandan A, Chuang F-C, Chueh Y-L (2020) Hybridizing plasmonic materials with 2d-transition metal dichalcogenides toward functional applications. *Small* 16:1904271. <https://doi.org/10.1002/sml.201904271>
- [10] Long X, Wang Z, Xiao S, An Y, Yang S (2016) Transition metal based layered double hydroxides tailored for energy conversion and storage. *Mater Today* 19:213. <https://doi.org/10.1016/j.mattod.2015.10.006>
- [11] Wang Y, Yan D, El Hankari S, Zou Y, Wang S (2018) Recent progress on layered double hydroxides and their derivatives for electrocatalytic water splitting. *Adv Sci* 5:1800064. <https://doi.org/10.1002/advs.201800064>
- [12] Trotochaud L, Young SL, Ranney JK, Boettcher SW (2014) Nickel-iron oxyhydroxide oxygen-evolution electrocatalysts: the role of intentional and incidental iron incorporation. *J Am Chem Soc* 136:6744. <https://doi.org/10.1021/ja502379c>
- [13] Chen JYC, Dang L, Liang H, Bi W, Gerken JB, Jin S, Alp EE, Stahl SS (2015) Operando analysis of NiFe and Fe oxyhydroxide electrocatalysts for water oxidation: detection of Fe^{4+} by mössbauer spectroscopy. *J Am Chem Soc* 137:15090. <https://doi.org/10.1021/jacs.5b10699>
- [14] Liu Y, Liang X, Gu L, Zhang Y, Li G-D, Zou X, Chen J-S (2018) Corrosion engineering towards efficient oxygen evolution electrodes with stable catalytic activity for over 6000 hours. *Nat Commun* 9:2609. <https://doi.org/10.1038/s41467-018-05019-5>
- [15] Zhong DK, Sun J, Inumaru H, Gamelin DR (2009) Solar water oxidation by composite catalyst/ $\alpha\text{-Fe}_2\text{O}_3$ photoanodes. *J Am Chem Soc* 131:6086. <https://doi.org/10.1021/ja9016478>
- [16] Lu X, Zhao C (2015) Electrodeposition of hierarchically structured three-dimensional nickel-iron electrodes for efficient oxygen evolution at high current densities. *Nat Commun* 6:6616. <https://doi.org/10.1038/ncomms7616>
- [17] Chen J, Zheng F, Zhang S-J, Fisher A, Zhou Y, Wang Z, Li Y, Xu B-B, Li J-T, Sun S-G (2018) Interfacial interaction between FeOOH and Ni-Fe LDH to modulate the local electronic structure for enhanced OER electrocatalysis. *ACS Catal* 8:11342. <https://doi.org/10.1021/acscatal.8b03489>
- [18] Shang X, Yan K-L, Lu S-S, Dong B, Gao W-K, Chi J-Q, Liu Z-Z, Chai Y-M, Liu C-G (2017) Controlling electrodeposited ultrathin amorphous Fe hydroxides film on V-doped nickel sulfide nanowires as efficient electrocatalyst for water oxidation. *J Pow Sour* 363:44. <https://doi.org/10.1016/j.jpowsour.2017.07.056>
- [19] Liu Z, Yu C, Han X, Yang J, Zhao C, Huang H, Qiu J (2016) CoMn layered double hydroxides/carbon nanotubes architectures as high-performance electrocatalysts for the oxygen

- evolution reaction. *ChemElectroChem* 3:906. <https://doi.org/10.1002/celec.201600116>
- [20] Li X, Zai J, Liu Y, He X, Xiang S, Ma Z, Qian X (2016) Atomically thin layered NiFe double hydroxides assembled 3D microspheres with promoted electrochemical performances. *J Pow Sour* 325:675. <https://doi.org/10.1016/j.jpowsour.2016.06.090>
- [21] Feng Y, Zhang H, Fang L, Mu Y, Wang Y (2016) Uniquely monodispersing NiFe alloyed nanoparticles in three-dimensional strongly linked sandwiched graphitized carbon sheets for high-efficiency oxygen evolution reaction. *ACS Catal* 6:4477. <https://doi.org/10.1021/acscatal.6b00481>
- [22] Yu J, Yang F, Cheng G, Luo W (2018) Construction of a hierarchical NiFe layered double hydroxide with a 3D mesoporous structure as an advanced electrocatalyst for water oxidation. *Inorg Chem Front* 5:1795. <https://doi.org/10.1039/C8QI00314A>
- [23] Liu J, Wang J, Zhang B, Ruan Y, Lv L, Ji X, Xu K, Miao L, Jiang J (2017) Hierarchical NiCo₂S₄@NiFe LDH heterostructures supported on nickel foam for enhanced overall-water-splitting activity. *ACS Appl Mater Inter* 9:15364. <https://doi.org/10.1021/acscami.7b00019>
- [24] Zou X, Liu Y, Li G-D, Wu Y, Liu D-P, Li W, Li H-W, Wang D, Zhang Y, Zou X (2017) Ultrafast formation of amorphous bimetallic hydroxide films on 3D conductive sulfide nanoarrays for large-current-density oxygen evolution electrocatalysis. *Adv Mater* 29:1700404. <https://doi.org/10.1002/adma.201700404>
- [25] Luo Y, Tang L, Khan U, Yu Q, Cheng H-M, Zou X, Liu B (2019) Morphology and surface chemistry engineering toward pH-universal catalysts for hydrogen evolution at high current density. *Nat Commun* 10:269. <https://doi.org/10.1038/s41467-018-07792-9>
- [26] Li H, Chen S, Zhang Y, Zhang Q, Jia X, Zhang Q, Gu L, Sun X, Song L, Wang X (2018) Systematic design of super-aerophobic nanotube-array electrode comprised of transition-metal sulfides for overall water splitting. *Nat Commun* 9:2452. <https://doi.org/10.1038/s41467-018-04888-0>
- [27] Quéré D (2005) Non-sticking drops. *Rep Prog Phys* 68:2495. <https://doi.org/10.1088/0034-4885/68/11/r01>
- [28] Lai Y, Gao X, Zhuang H, Huang J, Lin C, Jiang L (2009) Designing superhydrophobic porous nanostructures with tunable water adhesion. *Adv Mater* 21:3799. <https://doi.org/10.1002/adma.200900686>
- [29] Chen J, Li B, Zheng J, Jia S, Zhao J, Jing H, Zhu Z (2011) Role of one-dimensional ribbonlike nanostructures in dye-sensitized TiO₂-based solar cells. *J Phys Chem C* 115:7104. <https://doi.org/10.1021/jp2004369>
- [30] Wang G, Wang H, Ling Y, Tang Y, Yang X, Fitzmorris RC, Wang C, Zhang JZ, Li Y (2011) Hydrogen-treated TiO₂ nanowire arrays for photoelectrochemical water splitting. *Nano Lett* 11:3026. <https://doi.org/10.1021/nl201766h>
- [31] Du C, Yang L, Yang F, Cheng G, Luo W (2017) Nest-like nicop for highly efficient overall water splitting. *ACS Catal* 7:4131. <https://doi.org/10.1021/acscatal.7b00662>
- [32] Song F, Hu X (2014) Exfoliation of layered double hydroxides for enhanced oxygen evolution catalysis. *Nat Commun* 5:4477. <https://doi.org/10.1038/ncomms5477>
- [33] Joensen P, Crozier ED, Alberding N, Frindt RF (1987) A study of single-layer and restacked MoS₂ by X-ray diffraction and X-ray absorption spectroscopy. *J Phys C Solid State Phys* 20:4043. <https://doi.org/10.1088/0022-3719/20/26/009>
- [34] Wang M, Xu C, Li C, Jin Y (2019) Self-supporting MOF-derived CoNi@C–Au/TiO₂ nanotube array Z-scheme heterocatalysts for plasmon-enhanced high-efficiency full water splitting. *J Mater Chem A* 7:19704. <https://doi.org/10.1039/C9TA07776F>
- [35] Gong M, Wang D-Y, Chen C-C, Hwang B-J, Dai H (2016) A mini review on nickel-based electrocatalysts for alkaline hydrogen evolution reaction. *Nano Res* 9:28. <https://doi.org/10.1007/s12274-015-0965-x>
- [36] Ding J, Li L, Wang Y, Li H, Yang M, Li G (2020) Topological transformation of LDH nanosheets to highly dispersed PtNiFe nanoalloys enhancing CO oxidation performance. *Nanoscale* 12:14882. <https://doi.org/10.1039/D0NR02272A>
- [37] Vassalini I, Borgese L, Mariz M, Polizzi S, Aquilanti G, Ghigna P, Sartorel A, Amendola V, Alessandri I (2017) Enhanced electrocatalytic oxygen evolution in Au–Fe nanoalloys. *Angew Chem Int Ed* 56:6589. <https://doi.org/10.1002/anie.201703387>
- [38] Zhang C, Liu Y, Chang Y, Lu Y, Zhao S, Xu D, Dai Z, Han M, Bao J (2017) Component-controlled synthesis of necklace-like hollow Ni_xRu_y nanoalloys as electrocatalysts for hydrogen evolution reaction. *ACS Appl Mater Inter* 9:17326. <https://doi.org/10.1021/acscami.7b01114>
- [39] Nair AS, Pathak B (2021) Computational strategies to address the catalytic activity of nanoclusters. *WIREs Comput Mol Sci* 11:e1508. <https://doi.org/10.1002/wcms.1508>
- [40] Asnavandi M, Zhao C (2017) Autologous growth of nickel oxyhydroxides with in situ electrochemical iron doping for efficient oxygen evolution reactions. *Mater Chem Front* 1:2541. <https://doi.org/10.1039/C7QM00367F>
- [41] Li X, Hao X, Wang Z, Abudula A, Guan G (2017) In-situ intercalation of NiFe LDH materials: an efficient approach to improve electrocatalytic activity and stability for water splitting. *J Pow Sour* 347:193. <https://doi.org/10.1016/j.jpowsour.2017.02.062>
- [42] Jia Y, Zhang L, Gao G, Chen H, Wang B, Zhou J, Soo MT, Hong M, Yan X, Qian G, Zou J, Du A, Yao X (2017) A

- heterostructure coupling of exfoliated Ni–Fe hydroxide nanosheet and defective graphene as a bifunctional electrocatalyst for overall water splitting. *Adv Mater* 29:1700017. <https://doi.org/10.1002/adma.201700017>
- [43] Jiang X-X, Xue J-Y, Zhao Z-Y, Li C, Li F-L, Cao C, Niu Z, Gu H-W, Lang J-P (2020) Ultrathin sulfate-intercalated NiFe-layered double hydroxide nanosheets for efficient electrocatalytic oxygen evolution. *RSC Adv* 10:12145. <https://doi.org/10.1039/d0ra00845a>
- [44] Cui M, Yang C, Li B, Dong Q, Wu M, Hwang S, Xie H, Wang X, Wang G, Hu L (2020) High-entropy metal sulfide nanoparticles promise high-performance oxygen evolution reaction. *Adv Energy Mater.* <https://doi.org/10.1002/aenm.202002887>
- [45] Meng X, Han J, Lu L, Qiu G, Wang ZL, Sun C (2019) Fe²⁺-doped layered double (Ni, Fe) hydroxides as efficient electrocatalysts for water splitting and self-powered electrochemical systems. *Small* 15:1902551. <https://doi.org/10.1002/sml.201902551>
- [46] Nai J, Lu Y, Yu L, Wang X, Lou XW (2017) Formation of Ni–Fe mixed diselenide nanocages as a superior oxygen evolution electrocatalyst. *Adv Mater* 29:1703870. <https://doi.org/10.1002/adma.201703870>
- [47] Dong C, Kou T, Gao H, Peng Z, Zhang Z (2018) Eutectic-derived mesoporous Ni-Fe-O nanowire network catalyzing oxygen evolution and overall water splitting. *Adv Energy Mater* 8:1701347. <https://doi.org/10.1002/aenm.201701347>
- [48] Zhang X, Xu H, Li X, Li Y, Yang T, Liang Y (2016) Facile synthesis of nickel–iron/nanocarbon hybrids as advanced electrocatalysts for efficient water splitting. *ACS Catal* 6:580. <https://doi.org/10.1021/acscatal.5b02291>
- [49] Piontek S, Andronesu C, Zaichenko A, Konkona B, Puring KJ, Marler B, Antoni H, Sinev I, Muhler M, Mollenhauer D, Cuenya BR, Schuhmann W, Apfel U-P (2018) Influence of the Fe: Ni ratio and reaction temperature on the efficiency of (Fe_xNi_{1-x})₉S₈ electrocatalysts applied in the hydrogen evolution reaction. *ACS Catal* 8:987. <https://doi.org/10.1021/acscatal.7b02617>
- [50] Babar P, Lokhande A, Shin HH, Pawar B, Gang MG, Pawar S, Kim JH (2018) Cobalt iron hydroxide as a precious metal-free bifunctional electrocatalyst for efficient overall water splitting. *Small* 14:1702568. <https://doi.org/10.1002/sml.201702568>
- [51] Laurens LML, Markham J, Templeton DW, Christensen ED, Van Wycken S, Vadelius EW, Chen-Glasser M, Dong T, Davis R, Pienkos PT (2017) Development of algae biorefinery concepts for biofuels and bioproducts; a perspective on process-compatible products and their impact on cost-reduction. *Energy Environ Sci* 10:1716. <https://doi.org/10.1039/C7EE01306J>
- [52] Zhang H, Li X, Hähnel A, Naumann V, Lin C, Azimi S, Schweizer SL, Maijenburg AW, Wehrspohn RB (2018) Bifunctional heterostructure assembly of NiFe LDH nanosheets on NiCoP nanowires for highly efficient and stable overall water splitting. *Adv Funct Mater* 28:1706847. <https://doi.org/10.1002/adfm.201706847>
- [53] Dinh KN, Zheng P, Dai Z, Zhang Y, Dangol R, Zheng Y, Li B, Zong Y, Yan Q (2018) Ultrathin porous NiFeV ternary layer hydroxide nanosheets as a highly efficient bifunctional electrocatalyst for overall water splitting. *Small* 14:1703257. <https://doi.org/10.1002/sml.201703257>
- [54] Wang Z, Zeng S, Liu W, Wang X, Li Q, Zhao Z, Geng F (2017) Coupling molecularly ultrathin sheets of NiFe-layered double hydroxide on NiCo₂O₄ nanowire arrays for highly efficient overall water-splitting activity. *ACS Appl Mater Inter* 9:1488. <https://doi.org/10.1021/acscami.6b13075>
- [55] Rajeshkhanna G, Kandula S, Shrestha KR, Kim NH, Lee JH (2018) A new class of Zn_{1-x}Fe_x-oxyselenide and Zn_{1-x}Fe_x-LDH nanostructured material with remarkable bifunctional oxygen and hydrogen evolution electrocatalytic activities for overall water splitting. *Small* 14:1803638. <https://doi.org/10.1002/sml.201803638>
- [56] Luo J, Im JH, Mayer MT, Schreier M, Nazeeruddin MK, Park NG, Tilley SD, Fan HJ, Gratzel M (2014) Water photolysis at 12.3% efficiency via perovskite photovoltaics and earth-abundant catalysts. *Science* 345:1593. <https://doi.org/10.1126/science.1258307>
- [57] Feng L-L, Yu G, Wu Y, Li G-D, Li H, Sun Y, Asefa T, Chen W, Zou X (2015) High-Index faceted Ni₃S₂ nanosheet arrays as highly active and ultrastable electrocatalysts for water splitting. *J Am Chem Soc* 137:14023. <https://doi.org/10.1021/jacs.5b08186>

Publisher's Note Springer Nature remains neutral with regard to jurisdictional claims in published maps and institutional affiliations.